

Article

Glycyrrhiza uralensis Nodules: Histological and Ultrastructural Organization and Tubulin Cytoskeleton Dynamics

Anna V. Tsyganova ¹, Anna B. Kitaeva ¹, Artemii P. Gorshkov ¹, Pyotr G. Kusakin ¹, Alexandra R. Sadovskaya ², Yaroslav G. Borisov ² and Viktor E. Tsyganov ^{1,3,*}

¹ Laboratory of Molecular and Cellular Biology, All-Russia Research Institute for Agricultural Microbiology, 196608 Saint Petersburg, Russia; avtsyganova@arriam.ru (A.V.T.); anykitaeva@gmail.com (A.B.K.); artemius1993@yandex.ru (A.P.G.); kussakin@gmail.com (P.G.K.)

² Faculty of Biology, Saint Petersburg State University, 199034 Saint Petersburg, Russia; alexandrasad@mail.ru (A.R.S.); gis.ib88@gmail.com (Y.G.B.)

³ Saint Petersburg Scientific Center RAS, 199034 Saint Petersburg, Russia

* Correspondence: vetsyganov@arriam.ru; Tel.: +7-812-4705100

Abstract: Chinese liquorice (*Glycyrrhiza uralensis* Fisch. ex DC.) is widely used in the food industry and as a medicine. Like other legumes, *G. uralensis* forms symbiotic nodules. However, the structural organization of *G. uralensis* nodules is poorly understood. In this study, we analyzed the histological and ultrastructural organization and dynamics of the tubulin cytoskeleton in various cells from different histological zones of indeterminate nodules formed by two strains of *Mesorhizobium* sp. The unusual walls of infection threads and formation of multiple symbiosomes with several swollen bacteroids were observed. A large amount of poly- β -hydroxybutyrate accumulated in the bacteroids, while the vacuoles of meristematic and uninfected cells contained drop-shaped osmiophilic inclusions. Immunolocalization of the tubulin cytoskeleton and quantitative analysis of cytoskeletal elements revealed patterns of cortical microtubules in meristematic, infected and uninfected cells, and of endoplasmic microtubules associated with infection structures, typical of indeterminate nodules. The intermediate pattern of endoplasmic microtubules in infected cells was correlated with disordered arrangement of symbiosomes. Thus, analysis of the structural organization of *G. uralensis* nodules revealed some ancestral features more characteristic of determinate nodules, demonstrating the evolutionary closeness of *G. uralensis* nodulation to more ancient members of the legume family.

Keywords: legume-rhizobial symbiosis; indeterminate nodules; infection thread; bacteroid; symbiosomes; microtubules



Citation: Tsyganova, A.V.; Kitaeva, A.B.; Gorshkov, A.P.; Kusakin, P.G.; Sadovskaya, A.R.; Borisov, Y.G.; Tsyganov, V.E. *Glycyrrhiza uralensis* Nodules: Histological and Ultrastructural Organization and Tubulin Cytoskeleton Dynamics. *Agronomy* **2021**, *11*, 2508. <https://doi.org/10.3390/agronomy11122508>

Academic Editor: Alberto San Bautista

Received: 5 November 2021

Accepted: 7 December 2021

Published: 10 December 2021

Publisher's Note: MDPI stays neutral with regard to jurisdictional claims in published maps and institutional affiliations.



Copyright: © 2021 by the authors. Licensee MDPI, Basel, Switzerland. This article is an open access article distributed under the terms and conditions of the Creative Commons Attribution (CC BY) license (<https://creativecommons.org/licenses/by/4.0/>).

1. Introduction

Legumes are able to form symbioses with both arbuscular mycorrhiza fungi and nodule bacteria (rhizobia) [1]. Studying legume symbioses with rhizobia is of great interest for agriculture; the use of biological nitrogen fixation leads to a reduction in the use of mineral nitrogen fertilizers, improvements in the physical properties of the soil, increased soil biodiversity, and thus a beneficial effect on the environment [2,3]. Legumes are widely used in agriculture, comprising the main food crops in some areas [4]. Their particular importance is due to their high protein content; however, some legumes can also produce phytochemicals, which are plant secondary metabolites of great interest for practical use. One such plant is Chinese liquorice (*Glycyrrhiza uralensis*).

G. uralensis is a perennial herbaceous legume that is actively used in the medical and food industries. *G. uralensis* produce triterpene saponins, flavonoids and polysaccharides [5–7]. This plant is actively being studied due to its economic importance; the analysis of its transcriptome [8,9], and the assembly and annotation of its draft genome [10], and complete chloroplast [11] and mitochondrial [12] genomes, have been carried out to date. Recently,

the effects of different stressors on transcriptome activity in *G. uralensis* plants have also been analyzed [13,14].

Upon inoculation with rhizobia, *G. uralensis* is able to form indeterminate nodules with prolonged meristem activity [15]. Extensive research has revealed that several rhizobial species (*Mesorhizobium tianshanense*, *M. mediterraneum* and other *Mesorhizobium* sp.) can be considered true symbionts of *G. uralensis*, and sporadic nitrogen-fixing nodules can also be formed by different rhizobial species (*Rhizobium galegae*, *R. leguminosarum*, *Sinorhizobium meliloti* and some others) [16].

Although *G. uralensis* is an important legume crop, the mechanisms of its interactions with rhizobia are still poorly understood. Descriptions of the structural organization of symbiotic nodules are very limited [17,18]. Indeterminate nodules form several histological zones, including the meristem, the zone of infection, and the zone of nitrogen fixation, and, with increasing age of the nodules, the senescence zone [19]. The formation of a nitrogen fixation zone is a prerequisite for beneficial symbioses; at the same time, the premature formation of the senescence zone indicates ineffective symbiosis [20], which can be caused both by inoculation with an ineffective rhizobia strain [21–23] and by unfavorable environmental factors [24–26].

In effective indeterminate nodules, infected cells are filled with symbiosomes containing a single bacteroid [27,28]. However, the morphology of bacteroids in the symbiosomes varies considerably and several morphotypes have been distinguished. In some legumes, such as *Medicago sativa* and *Galega orientalis*, bacteroids are elongated and not branched (ENB morphotype) [29,30]; in others, such as *Pisum sativum* and *Vicia sativa*, they are elongated and branched (EB morphotype) or even pleiomorphic [30,31]; finally, swollen and spherical (S morphotype) bacteroids are typical for *Cicer arietinum* [30,32]. For determinate nodules, undifferentiated bacteroids (U morphotype) are typical [33].

Bacteroid morphology in *G. uralensis* nodules formed by *M. tianshanense* (HAMBI 3372) was classified only recently as U morphotype [33]. Later, Montiel and colleagues suggested a modified classification system for bacteroid morphotypes; they distinguished swollen (S), elongated (E), spherical (SP), and elongated–branched (EB) [32]. According to their classification, bacteroids in *G. uralensis* nodules are of the S morphotype, which correlated with a low quantity of nodule cysteine-rich (NCR) peptides [32].

G. uralensis is undoubtedly of great interest for studies of tubulin cytoskeletal organization in nodules. Studies of microtubular organization in indeterminate nodules in several legume species with different bacteroid morphotypes have been carried out previously, but only for S morphotype bacteroids in *C. arietinum* [30,34].

A detailed understanding of the symbiotic nodule formation mechanism in *G. uralensis* has important practical value, because it was recently shown that symbiotic nodule formation led to increases in plant biomass and glycyrrhizin production [35]. It is interesting to note that the interaction of *G. uralensis* plants with mycorrhizal fungi has been shown previously to have a positive effect on the production of glycyrrhizin and liquiritin [36,37].

This study therefore aimed to establish the histological and ultrastructural organization of nodules formed upon inoculation of *G. uralensis* with two strains of *Mesorhizobium* sp. Using one of the strains, the dynamics of the tubulin cytoskeleton in the cells of various histological zones of the *G. uralensis* nodule were also investigated.

2. Materials and Methods

2.1. Plant Material, Bacteria Strains and Growth Conditions

Commercial seeds of *Glycyrrhiza uralensis* Fisch. ex DC. (“Baikal Herbs” Ltd., Irkutsk, Russia) were used. Seeds were sterilized in concentrated sulfuric acid for 15 min, followed by washing in sterile water 10 times, and germination at 28 °C. For inoculation, effective *Mesorhizobium* sp. strains RCAM3115 and RCAM3120 from the Russian Collection of Agricultural Microorganisms (All-Russia Research Institute for Agricultural Microbiology, Saint Petersburg, Russia) were used. Four independent experiments were performed.

Plants were grown in sterile vermiculite wetted with nitrogen-free nutrient solution [38], in an MLR-352H growth chamber (Sanyo Electric Co., Ltd., Moriguchi, Japan) under controlled conditions: day/night, 16/8; temperature 21 °C; humidity 75%; illumination 280 $\mu\text{mol photons m}^{-2} \text{s}^{-1}$. Nodules were harvested in two weeks after the inoculation.

2.2. Microscopy

2.2.1. Light Microscopy

Approximately 10–15 nodules were harvested from different plants and placed directly into fixative; a lateral cut was made on each nodule to improve penetration of the fixative. The nodules were fixed in 2.5% glutaraldehyde (Sigma-Aldrich, St. Louis, MO, USA) in 0.01% phosphate buffered saline (PBS; 2.48 g/L NaH_2PO_4 , 21.36 g/L Na_2HPO_4 , and 87.66 g/L NaCl, pH 7.2). Then, the samples were placed under vacuum to remove air from the intercellular spaces and were left in fixative overnight at 4 °C.

The nodules were washed in buffer (four times for 15 min each) and postfixed in 2% osmium tetroxide in 0.1 M phosphate buffer for 2 h. The samples were dehydrated as described previously [20]. Dehydrated samples were progressively infiltrated with Eponate 12 (Ted Pella, Inc., Redding, CA, USA) at room temperature. Finally, samples were embedded in fresh Eponate 12 resin, which was polymerized at 60 °C for 48 h in small plastic containers. Dehydration and resin embedding of the samples was carried out using an Automated Tissue Processor Leica EM TP (Leica Microsystems, Vienna, Austria).

For light microscopy, the embedded material was cut into semi-thin sections (1 μm) using a Leica EM UC7 ultramicrotome (Leica Microsystems). Sections were placed on SuperFrost glass slides (Menzel-Gläser, Thermo Fisher Scientific, Waltham, MA, USA) and stained with methylene blue-azure II for 20 min at 65 °C [39]. Sections were examined under an Axio Imager.Z1 microscope (Zeiss, Oberkochen, Germany) and images were acquired using an Axiocam 506 digital video camera (Zeiss).

2.2.2. Transmission Electron Microscopy

For transmission electron microscopy, ultrathin sections (90–100 nm thick) were cut with a Leica EM UC7 ultramicrotome (Leica Microsystems) and counterstained as described previously [20]. Nodule tissues were examined using a JEM-1200 EM transmission electron microscope (JEOL Ltd., Tokyo, Japan) at 80 kV. Electron micrographs were captured using a Veleta CCD camera (Olympus, Münster, Germany).

2.2.3. Scanning Electron Microscopy

Nodules were fixed in 2.5% glutaraldehyde in phosphate buffer (0.06 M, pH 7.2). The nodules were dehydrated with a graded ethanol series and dried with a critical point dryer Leica EM CPD300 (Leica Microsystems). Then, specimens were mounted on stubs, coated with 20 nm gold using a high vacuum sputter coater Leica EM SCD500 (Leica Microsystems) and observed in a Tescan MIRA3 LMU scanning electron microscope (Tescan, Brno, Czech Republic) at 9 kV.

2.2.4. Immunolocalization

Visualization of tubulin microtubules was performed according to a previously described technique [34] with some necessary modifications according to the specificity of every plant species [40]. Nodules were fixed in 1/4 microtubule stabilizing buffer [MTSB] (50 mM piperazine-*N,N'*-bis[2-ethanesulfonic acid] [PIPES], 5 mM $\text{MgSO}_4 \cdot 7\text{H}_2\text{O}$, 5 mM egtazic acid [EGTA], pH 6.9) containing 3% formaldehyde, 0.25% glutaraldehyde, 0.3% Tween-20, 0.3% Triton X-100, and 10% dimethyl sulfoxide. Air from tissues was pumped out for 15 min at -0.9 bar using a Vacuubrand ME 1C vacuum pump (Vacuubrand, Wertheim, Germany) seven times. Nodule longitudinal sections were taken using a HM650V microtome with a vibrating blade (Microm, Walldorf, Germany). A monoclonal mouse anti-tubulin IgG antibody (clone DM1A; Sigma-Aldrich) was used in a 1:1000 di-

lution, followed by an anti-mouse goat IgG secondary antibody conjugated with Alexa Fluor 488, diluted 1:500 (Thermo Fisher Scientific). Visualization of infection droplets and infection threads was performed using monoclonal rat antibody MAC265 (diluted 1:100) [41], followed by an anti-rat goat IgG secondary antibody conjugated with Alexa Fluor 546, diluted 1:500 (Thermo Fisher Scientific). To identify nuclei and bacteria, sections were stained with propidium iodide ($1 \mu\text{g mL}^{-1}$) for 7 min. Prior staining with propidium iodide, sections were incubated in RNase A solution (Thermo Fisher Scientific) in a 1:10 dilution for 30 min at 28 °C. After this, all sections were placed under coverslips in ProLong Diamond® antifade reagent (Thermo Fisher Scientific). Microtubule pattern analysis in nodule cells was performed using an LSM 780 laser scanning confocal microscope and ZEN 2012 software (Zeiss). AlexaFluor 488 was excited at 488 nm, and fluorescence emitted between 499 and 543 nm; Alexa Fluor 546 was excited at 561 nm, and emitted fluorescence between 568 and 572 nm; propidium iodide was excited at 561 nm, and emitted fluorescence between 606 and 677 nm.

2.2.5. Bacteroid Isolation

Five nodules were cut into pieces with a razor blade. Next, pieces of the nodules were digested in a 3% solution of cellulase from *Trichoderma viride* (Sigma-Aldrich) in 50 mM sodium-acetic buffer (Thermo Fisher Scientific) for 30 min at 28 °C, then stained with propidium iodide ($5 \mu\text{g mL}^{-1}$) for 15 min and ground with a glass pestle in 100 μL Tris-buffered saline. A quantity of 20 μL of suspension was mixed with 20 μL ProLong Diamond® antifade reagent (Thermo Fisher Scientific) on a glass slide and covered with a coverslip. Overall, the length of 50 bacteroids was determined.

2.2.6. Free-Living Bacteria Visualization

Bacterial cells were visualized according to a technique described by Montiel and colleagues [33] with some additions. Bacteria were heat treated at 70 °C for 2 h in a TT-2-Termit incubator (DNA-technology, Moscow, Russia) and stained with propidium iodide ($5 \mu\text{g mL}^{-1}$) for 15 min. A quantity of 20 μL of suspension was mixed with 20 μL ProLong Glass® antifade reagent (Thermo Fisher Scientific). Overall, the length of 25 bacteria was determined. Comparisons of bacteroid length were carried out using Student's *t*-test.

2.3. Quantitative Analysis

An analysis of cortical microtubule orientation was carried out as described previously [40] with modifications: full z-stack confocal images of individual nodule cells with labeled microtubules were converted to maximum intensity projections and binarized using the Phansalkar local thresholding algorithm [42] available in ImageJ software [43]. Using the MicroFilament Analyzer [44] program, tables with orientations of detected microtubules were obtained for each image. The frequencies for each angle were determined as a percentage, and the mean value for each cell was calculated using a custom R script. Angles were divided into 3 classes of 60 degrees each: axial ($0\text{--}30^\circ$, $150\text{--}180^\circ$), oblique ($30\text{--}60^\circ$, $120\text{--}150^\circ$) and transverse ($60\text{--}120^\circ$). Statistically significant differences in angle frequencies between the cell types were determined using Kruskal–Wallis and Dunn's tests.

Analysis of the endoplasmic microtubule distribution on full z-stack images was carried out as described previously [30] with the addition of 3 passes of ImageJ Remove Outliers median filter on black pixels for better image denoising. Additionally, isolation of endoplasmic microtubules in the images was performed using ImageJ functionality (ROI Manager and Clear Outside function) and macro language.

3. Results

3.1. Nodule Morphology

G. uralensis formed indeterminate nodules of round or elongated shape and 1.5–2 mm of length (Figure 1A) with zones typical of indeterminate nodules: meristem (zone I), infection (zone II), and nitrogen fixation (zone III) (Figure 1B). Both *Mesorhizobium* sp.

strains RCAM3115 (Figure S1A) and RCAM3120 (Figure S1B) formed nodules with similar histological organization.

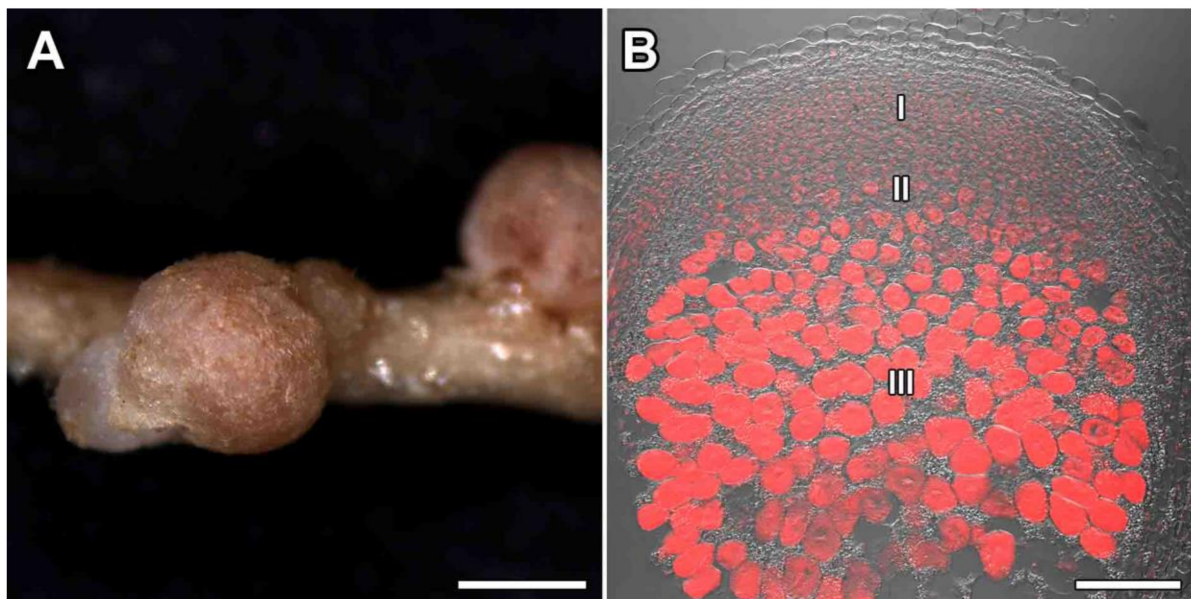


Figure 1. Nodulation of *Glycyrrhiza uralensis* Fisch. ex DC. (A) mature nodules; (B) histological organization of *Glycyrrhiza uralensis* nodules. I—meristem, II—zone of infection, III—zone of nitrogen fixation. Bar (A) = 1 mm, (B) = 500 μ m.

3.1.1. Meristem

The meristem of nitrogen-fixing nodules formed with both strains of *Mesorhizobium* sp. in *G. uralensis* was represented by small cells of irregular shape (Figure 2A–E). The cells in the center each contained a large nucleus with a prominent nucleolus and numerous small vacuoles. In vacuoles of the meristematic cells (Figure 2A,B,D,E), and uninfected cells from the infection zone (Figure 3A,B,D,E) and the nitrogen fixation zone (Figure 4F,G), drop-shaped inclusions of various sizes were found adjacent to the tonoplast. In addition to drop-shaped inclusions, finely dispersed material filling the vacuoles of meristematic cells was found (Figure 2B). Also found were meristematic cells with vacuoles that were completely filled with osmiophilic inclusions (Figure 2C). It was also possible to observe small vesicles with similar inclusions targeted towards the vacuole (Figure 2F).

3.1.2. Infection Zone

In the infection zone of *G. uralensis* nodules, numerous infection threads (Figure 3A–E) and infection droplets (Figure 3A–D,F) were observed. Infection threads and droplets had structures characteristic of those in other legumes; however, the wall of infection threads was noticeably different from the cell wall in density and fibrillarity (Figure 3E). The bacteria being released from the infection droplets were each surrounded by a separate membrane (Figure 3F). In a thin layer of cytoplasm around the merging vacuoles, juvenile bacteroids were distinguished, which did not differ from bacteria in the size and density of their matrix (Figure 3C,F).

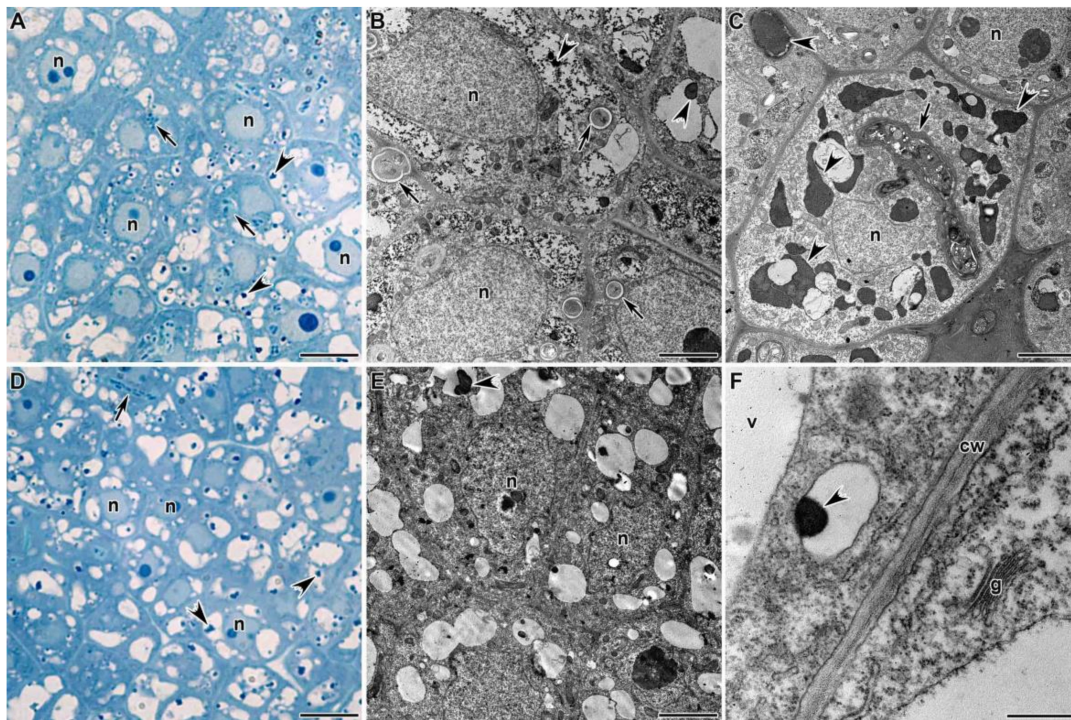


Figure 2. Histological and ultrastructural organization of the meristem in *Glycyrrhiza uralensis* Fisch. ex DC. nodules infected with *Mesorhizobium* sp. strains RCAM3115 (A–C) and RCAM3120 (D–F). n—nucleus, v—vacuole, cw—cell wall, g—Golgi apparatus. Arrows indicate infection threads, arrowheads indicate inclusions in vacuoles. Bar (A,D) = 5 μ m, (B,C,E) = 2 μ m, (F) = 500 nm.

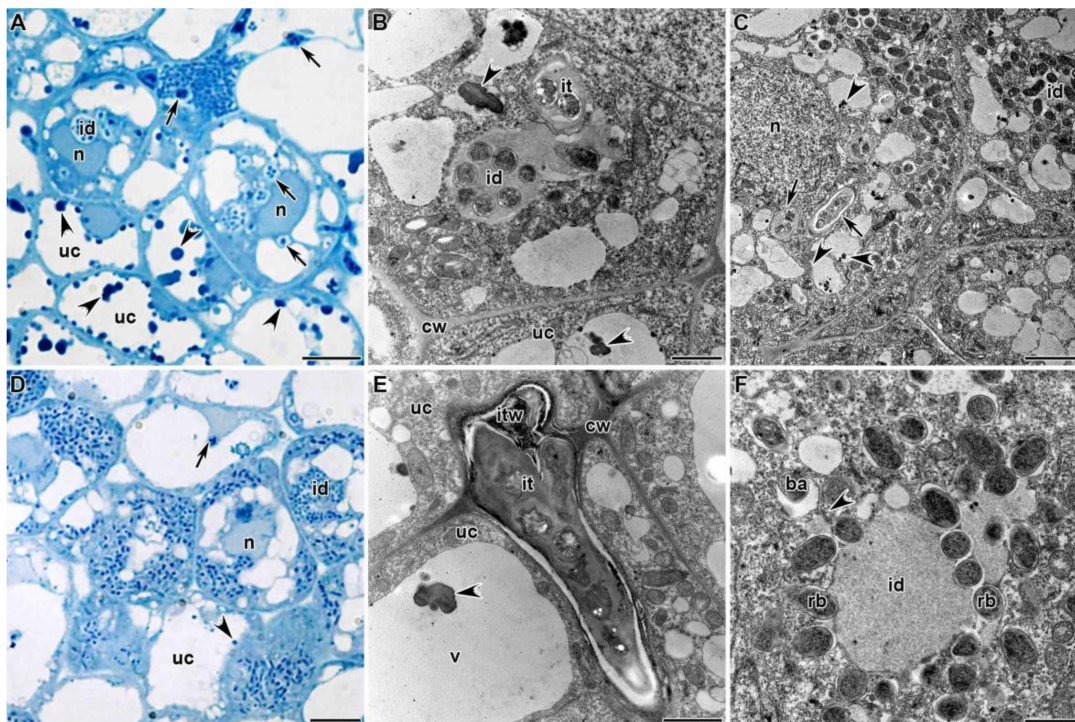


Figure 3. Histological and ultrastructural organization of the infection zone in *Glycyrrhiza uralensis* Fisch. ex DC. nodules infected with *Mesorhizobium* sp. strains RCAM3115 (A–C) and RCAM3120 (D–F). uc—uninfected cell, n—nucleus, v—vacuole, cw—cell wall, it—infection thread, id—infection droplet, itw—infection thread wall, rb—releasing bacteria, ba—bacteroid. Arrows indicate infection threads, arrowheads indicate inclusions in vacuoles. Bar (A,D) = 5 μ m, (C) = 2 μ m, (B,E,F) = 1 μ m.

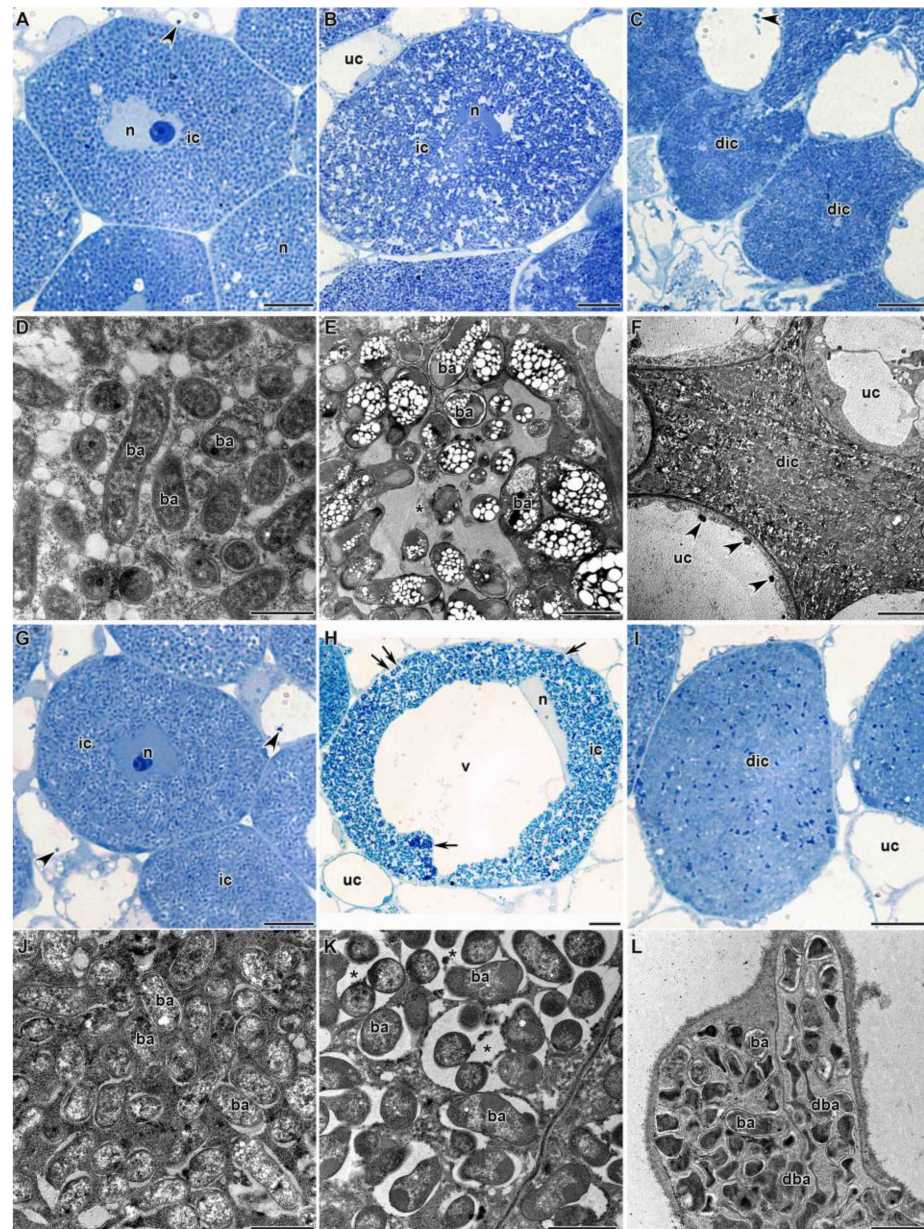


Figure 4. Histological and ultrastructural organization of the nitrogen fixation zone in *Glycyrrhiza uralensis* Fisch. ex DC. nodules infected with *Mesorhizobium* sp. strains RCAM3115 (A–F) and RCAM3120 (G–L): (A,G) young infected cells from the nitrogen fixation zone; (B,H) mature infected cells; (C,F,I,L) senescent infected cells; (D,J) symbiosomes with juvenile bacteroids; (E,K) symbiosomes with mature bacteroids. ic—infected cell, uc—uninfected cell, dic—degenerated infected cell, n—nucleus, v—vacuole, ba—bacteroid, dba—degenerated bacteroid, *—symbiosome with several bacteroids (‘multiple’ symbiosomes), arrows indicate multiple symbiosomes, arrowheads indicate inclusions in vacuoles. Bar (A–C,G–I) = 5 μ m, (F,L) = 2 μ m, (D,E,J,K) = 1 μ m.

3.1.3. Nitrogen Fixation Zone

In the nitrogen fixation zone, a gradient of differentiation was observed in the infected cells. Initially, young infected cells were filled with symbiosomes, each containing a single bacteroid (Figure 4D,J), with dense cytoplasm and a nucleus located in the center of the cell (Figure 4A,G). Further, mature infected cells were significantly increased in size compared with the young infected cells (Figure 4B,H). The central position in the cell was occupied by a vacuole, whereas the nucleus was tightly attached to the vacuole (Figure 4H). Symbiosomes in mature infected cells were increased in size compared with

the young infected cells due to the multiplication of bacteroids, and already contained several bacteroids, which could be observed both at the level of light microscopy (Figure 4H) and on electron microscopic micrographs (Figure 4E,K). Bacteroids in mature infected cells often contained numerous poly- β -hydroxybutyrate (PHB) granules, especially in the nodules formed by the strain RCAM3115 (Figure 4E). Further development of infected cells led to natural senescence, which in 2-week-old nodules was represented rarely among the cells (Figure 4C,I).

However, senescent cells looked different in nodules infected with the two different strains of rhizobia; upon inoculation with *Mesorhizobium* sp. strain RCAM3115, bacteroids fused in senescent infected cells, forming dense conglomerates (Figure 4C,F). With *Mesorhizobium* sp. strain RCAM3120, in contrast, individual bacteroids were observed in the senescent infected cells among the cleared degenerating bacteroids; their shape and the density of the matrix did not differ from free-living bacteria (Figure 4I,L).

The mature infected cells were filled with numerous rod-shaped bacteroids (Figure 5A,C) that can be classified as swollen (S morphotype). The S morphotype was confirmed by isolation and characterization of bacteroids (Figure 5B) and scanning electron microscopy of the nodules (Figure 5D). In nodules formed by *Mesorhizobium* sp. RCAM3120, the length of bacteroids was significantly increased ($2.39 \pm 0.0295 \mu\text{m}$) compared with the length of free-living bacteria ($1.15 \pm 0.0229 \mu\text{m}$, $p > 0.05$).

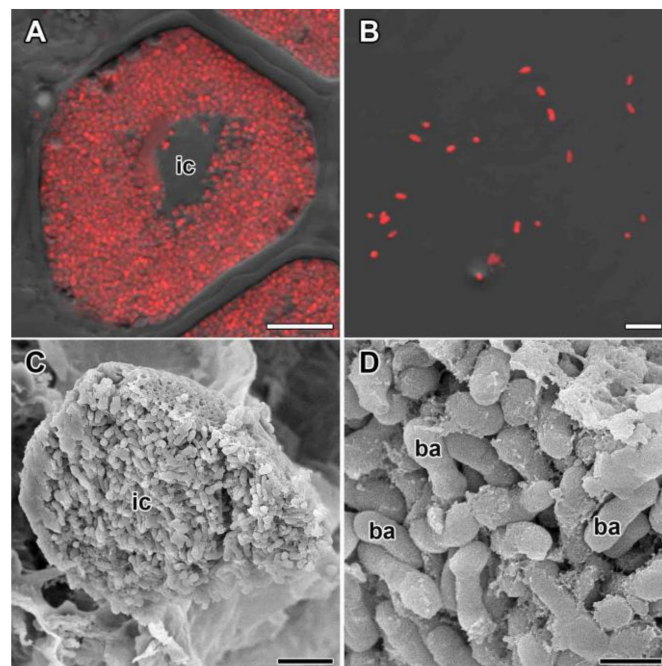


Figure 5. Infected cells and bacteroids in nodules of *Glycyrrhiza uralensis* Fisch. ex DC. (A,C) Symbiosome arrangement in infected cells of the nitrogen fixation zone; (B) bacteroid morphology based on laser scanning confocal microscopy; (D) bacteroid morphology based on scanning electron microscopy. (A,B) Merged images of differential interference contrast and red channel (DNA staining with propidium iodide [nuclei and bacteria]). ic—infected cell, ba—bacteroid. Bar (A–C) = 5 μm , (D) = 1 μm .

3.2. Microtubular Cytoskeleton

3.2.1. Meristematic Cells

In meristematic cells, the centrally located nucleus was surrounded by a dense net of perinuclear microtubules (Figure 6A,B). Thick bundles of endoplasmic microtubules connected the nucleus and the cell periphery. Cortical microtubules were located at different angles and criss-crossed, forming an irregular pattern (Figure 6A,B).

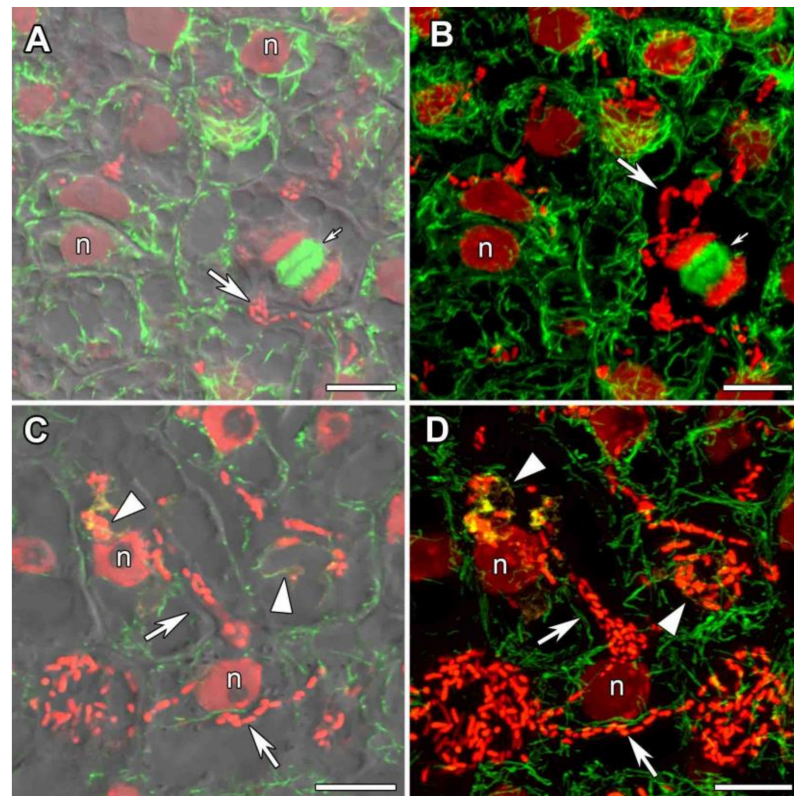


Figure 6. Microtubular organization in meristematic cells and in cells from the infection zone in nodules of *Glycyrrhiza uralensis* Fisch. ex DC. (A,B) Meristematic cells. (C,D) Cells from the infection zone. Confocal laser scanning microscopy of 35 μm longitudinal vibratome sections. Immunolocalization of tubulin (microtubules), green channel; DNA staining with propidium iodide (nuclei and bacteria), red channel; immunolocalization of MAC265 (infection droplets), yellow channel. (A) Merged images of a single optical section of differential interference contrast and green and red channels. (B) Maximum intensity projections of 25 optical sections in green and red channels. (C) Merged images of a single optical section of differential interference contrast and green, red and yellow channels. (D) Maximum intensity projections of 40 optical sections in green, red and yellow channels. n—nucleus. Triangles indicate infection droplets, large arrows indicate infection threads, small arrows indicate mitotic figures. Bars = 10 μm .

3.2.2. Cells of the Infection Zone

In the infection zone, the net of infection threads and infection droplets was easily distinguishable. Infected cells within the infection zone were characterized by an irregular pattern of cortical microtubules (Figure 6C,D, Video S1). Thick bundles of endoplasmic microtubules passed along infection threads, directing its growth, and surrounded the infection droplets (Figure 6C,D, Video S1).

3.2.3. Uninfected Cells

In *G. uralensis* nodules, uninfected cells, which lacked symbiosomes, were elongated. Cortical microtubules were mainly oriented parallel to one other and perpendicular to the longitudinal cell axis, forming a regular pattern (Figure 7A,B). Quantitative analysis confirmed that the majority of cortical microtubules were transversely oriented (Figure 7C).

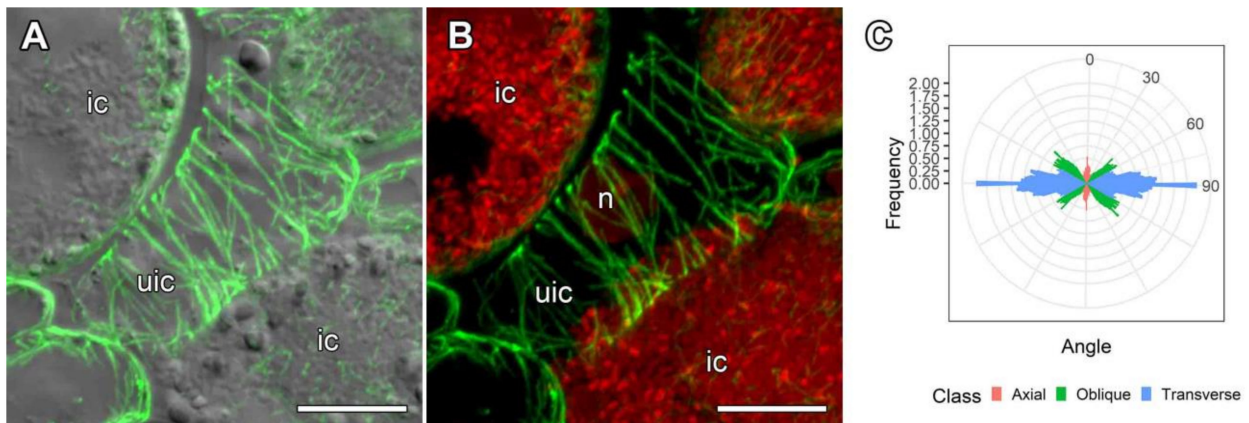


Figure 7. Organization and quantitative analysis of cortical microtubules in uninfected cells in nodules of *Glycyrrhiza uralensis* Fisch. ex DC. (A,B) Uninfected cells. Confocal laser scanning microscopy of 35 μm longitudinal vibratome sections. Immunolocalization of tubulin (microtubules), green channel; DNA staining with propidium iodide (nuclei and bacteria), red channel. (A) Merged images of a single optical section of differential interference contrast and maximum intensity projection of optical sections in the green channel. (B) Maximum intensity projections of 45 optical sections in the green and red channels. (C) Quantitative analysis of the organization of cortical microtubules in uninfected cells. Classes of microtubules: green—oblique, red—axial, blue—transverse. n—nucleus, ic—infected cell, uic—uninfected cell. Bars = 10 μm .

3.2.4. Infected Cells in the Nitrogen Fixation Zone

In infected cells, wavy bundles of endoplasmic microtubules located between symbiosomes were, to some extent, organized radially, but some randomly distributed microtubules were also present (Figure 8, Video S2). This pattern seemed to be intermediate between the regular and irregular patterns. Quantitative analysis was performed using six different parameters characterizing endoplasmic microtubule organization (Figure S2). Numerous symbiosomes were randomly distributed in the infected cells (Figures 5A,C and 8B). Cortical microtubules criss-crossed and formed an irregular pattern (Figure 9A,B, Video S3) which was statistically supported by quantitative analysis (Figure 9C).

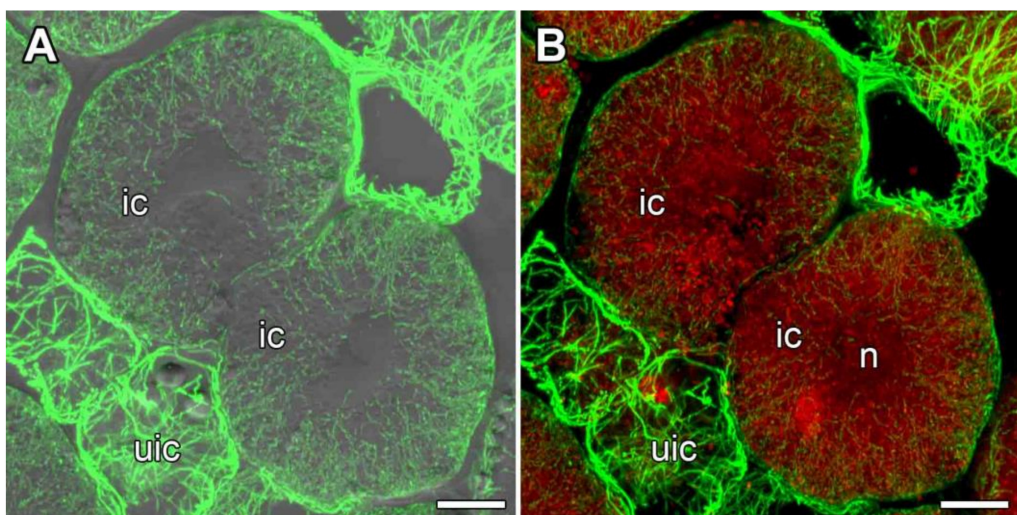


Figure 8. Organization of endoplasmic microtubules in infected cells in the nitrogen fixation zone in nodules of *Glycyrrhiza uralensis* Fisch. ex DC. Confocal laser scanning microscopy of 35 μm longitudinal vibratome sections. Immunolocalization of tubulin (microtubules), green channel; DNA staining with propidium iodide (nuclei and bacteria), red channel. (A) Merged images of a single optical section of differential interference contrast and maximum intensity projection of optical sections in the green channel. (B) Maximum intensity projections of 50 optical sections in the green and red channels. n—nucleus, ic—infected cell, uic—uninfected cell. Bars, 10 μm .

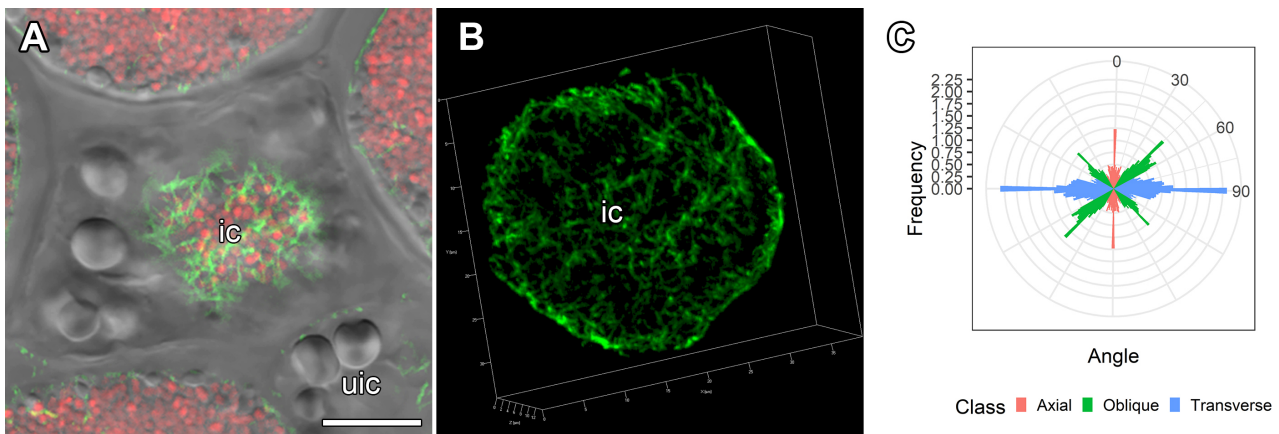


Figure 9. Organization of cortical microtubules in infected cells from the nitrogen fixation zone in nodules of *Glycyrrhiza uralensis* Fisch. ex DC. and their quantitative analysis. (A,B) Cells from the nitrogen fixation zone. Confocal laser scanning microscopy of 35 μm longitudinal vibratome sections. Immunolocalization of tubulin (microtubules), green channel; DNA staining with propidium iodide (nuclei and bacteria), red channel. (A) Merged images of a single optical section of differential interference contrast and green and red channels. (B) 3D reconstruction of 60 optical sections in the green channel. (C) Quantitative analysis of organization of cortical microtubules in infected cells. Classes of microtubules: green—oblique, red—axial, blue—transverse. ic—infected cell, uic—uninfected cell. Bars = 10 μm .

4. Discussion

Traditionally, legume root nodules are divided into two different types: determinate and indeterminate [19,45]. Determinate nodules are usually formed by legumes in (sub)tropical climates; they have a spherical shape, a temporary meristem, and do not exhibit histological zonation [19]. Indeterminate nodules are formed in legumes of the temperate zone, and are characterized by an elongated shape, a constant meristem, and thus histological zonation [19]. *G. uralensis* forms nodules of an indeterminate type; in our study, two types of nodules were observed: spherical and elongated. However, when examining the histological structure, it was shown that spherical nodules also belonged to the indeterminate type, with a pronounced histological zonation. Taking into consideration that we analyzed two-week-old nodules, it is possible that small spherical nodules represent young nodules. It was previously shown that, upon inoculation of *G. uralensis* plants with *S. fredii* HH103 [15,46] or *M. tianshanense* [33] strains, elongated [33] or even multilobed nodules were formed [15]; however, these studies analyzed four-week-old or six-week-old nodules and are therefore not directly comparable with our study.

The walls of the infection threads significantly differed from the cell walls, both in terms of density and fibrillar composition. They also looked different from the walls of the infection threads growing in nodules of *P. sativum* and *M. truncatula* [47,48]. Undoubtedly, further study of the composition of these infection thread walls in *G. uralensis* nodules is of great interest.

Another intriguing observation was that in mature nitrogen-fixing cells of the *G. uralensis* nodules, symbiosomes contained several bacteroids, which is generally not typical for indeterminate nodules [27,28,49]. Until now, only one exception to this rule was known: the woody legume *Leucaena glauca* forms indeterminate nodules in which the symbiosome contains several bacteroids [50]. However, during the formation of indeterminate nodules, the fusion of symbiosome membranes and thus the formation of ‘multiple’ symbiosomes is a common phenomenon, caused by unfavorable environmental conditions or plant mutations. For example, in *P. sativum* nodules, symbiosomes with several bacteroids were shown to be formed under cadmium stress [51,52] or treatment with the fungicide tetramethylthiuram disulfide (TMTD) [53]. In *M. truncatula* nodules, inactivation of the *Mtccs52A* (Cell cycle switch 52) gene, which encodes an activator of the anaphase complex [54], in addition to mutations in the *Rsd* (Regulator of symbiosome differentiation) gene [55], led to the formation of multiple symbiosomes. Similar phenotypes result from a knockdown of the

Rpf84 gene encoding RPL22 (ribosomal large subunit protein) in *Robinia pseudoacacia* [56]. In addition, many mutations in *P. sativum* symbiotic genes result in the formation of symbiosomes with several bacteroids, including those in *sym31* [57,58], *sym32* [59,60], *sym40*, and *sym33–3* [31,48]. *G. uralensis* has also been shown to be characterized by a low degree of differentiation in bacteroids [32,33], which belong either to the U (undifferentiated) [33] or S (swollen) morphotypes [32], which is consistent with this study. Previous studies have shown that *G. uralensis* is still capable of forming nitrogen-fixing nodules with lipopolysaccharide (LPS) and capsular polysaccharides (KPS) mutants of *S. fredii* HH103 [15,17,46], which is not typical of indeterminate nodules. For example, it is known that upon induction of indeterminate nodules by LPS mutants of *R. leguminosarum* bv. *viceae*, *M. loti*, *Sinorhizobium* sp. NGR234 and *S. meliloti*, sporadic bacterial endocytosis and early senescence of bacteroids is observed; at the same time, the division of bacteria in symbiosomes is disturbed, and its synchronization with the division of symbiosome membrane is absent, i.e., multiple symbiosomes are formed [46]. Thus, during nodulation in *G. uralensis*, some ancestral features characteristic of determinate nodules can be observed: poorly differentiated bacteroids and the formation of multiple symbiosomes [61]. It is worth noting that the genus *Glycyrrhiza* belongs to the most basal subclade of the inverted repeat-lacking clade (IRLC) [33].

In bacteroids formed by the strain RCAM3115, an increased accumulation of PHB was observed, which is characteristic of bacteroids in determinate nodules [62,63]. Another interesting feature of *G. uralensis* nodules is the presence of numerous drop-shaped inclusions in the vacuoles of meristematic and uninfected cells. Similar osmiophilic inclusions have been found in *Lotus pedunculatus* inoculated with the fast-growing rhizobia strain NZP2037 [64] and in *L. corniculatus* when exposed to heavy metals (nickel, cobalt, and chromium) [65]. Electron-dense osmiophilic deposits identified as flavolans [64] or phenolic compounds [65] were also present in the vacuoles of the outer cortical and epidermal cells, but not in the infected nodule cells. In *P. sativum* nodules exposed to high doses of TMTD, osmiophilic inclusions were also observed in the vacuoles of meristematic cells [53].

Our analysis of the tubulin cytoskeleton in cells in the *G. uralensis* nodules revealed irregular patterns of cortical microtubules in meristematic and infected cells, whereas uninfected cells had regular patterns. These observed patterns are typical of corresponding cells in indeterminate nodules [30,34]. Regular patterns of cortical microtubules lead to anisotropic growth, while irregular patterns are associated with isodiametric growth [66,67]. The organization of endoplasmic microtubules in meristematic cells and those associated with infection threads and droplets were typical of indeterminate nodules [30,34].

In infected *G. uralensis* cells, endoplasmic microtubules distributed among symbiosomes had an intermediate pattern, between regular and irregular patterns. In turn, symbiosomes were shown to have a disordered arrangement. Quantitative analysis showed similar endoplasmic microtubule organization between infected *G. uralensis* cells and those of *V. sativa* (compare Figure S2 and Figure 8 in [30]). Endoplasmic microtubules in infected *V. sativa* cells were also shown to form an intermediate pattern [30]. We have previously suggested that the arrangement of symbiosomes in a cell (ordered versus disordered) is determined by a regular or irregular pattern of endoplasmic microtubules, respectively. The formed endoplasmic microtubule pattern correlates with the shape and size of bacteroids. To a certain extent, similar coincidences were observed in analyses of five legume species that formed indeterminate nodules [30,34]. Although the sizes of the *G. uralensis* bacteroids are much smaller than those of *V. sativa* [30], the symbiosomes of *G. uralensis* contain several bacteroids; therefore, the size of the symbiosomes themselves in *G. uralensis* is much larger, and is comparable to the size of the symbiosomes in *V. sativa*. Moreover, *G. uralensis* symbiosomes are pleiomorphic, as are those in *V. sativa*.

5. Conclusions

In this study, for the first time, we produced a detailed characterization of the structure of *G. uralensis* nodules inoculated with *Mesorhizobium* sp. strains RCAM3115 and

RCAM3120. We demonstrated some ancestral features of nodulation in *G. uralensis*, characteristic of determinate nodules. These features include the formation of multiple symbiosomes containing several poorly-differentiated, rod-shaped bacteroids, and the accumulation of large amounts of PHB in mature bacteroids. Thus, these results can be useful for elucidating how plants with indeterminate nodules evolved from ancestor plants with determinate nodules.

Supplementary Materials: The following are available online at <https://www.mdpi.com/article/10.3390/agronomy11122508/s1>, Figure S1: Histological organization of *G. uralensis* nodules infected with *Mesorhizobium* sp. strains RCAM3115 and RCAM3120. Figure S2: Quantitative analysis of endoplasmic microtubules in nitrogen-fixing cells of *G. uralensis*. Video S1: Organization of endoplasmic and cortical microtubules in the infection zone of *G. uralensis* nodule. Video S2: Organization of endoplasmic microtubules in infected cell from the nitrogen fixation zone in *G. uralensis* nodule. Video S3: Organization of cortical microtubules in infected cell from the nitrogen fixation zone in *G. uralensis* nodule.

Author Contributions: Conceptualization, V.E.T. and A.V.T.; light microscopy and scan electron microscopy, A.V.T.; transmission electron microscopy, A.P.G.; confocal microscopy, A.B.K.; quantitative analysis of cytoskeleton, P.G.K. and A.R.S., electron microscopy resources, Y.G.B.; writing—original draft preparation, A.V.T.; writing—review and editing, V.E.T.; supervision, V.E.T.; project administration, A.B.K. All authors have read and agreed to the published version of the manuscript.

Funding: This research was funded by the Russian Foundation for Basic Research, grant number 20-316-70004.

Institutional Review Board Statement: Not applicable.

Informed Consent Statement: Not applicable.

Data Availability Statement: Not applicable.

Acknowledgments: This work was carried out using the equipment of the Core Centrum Genomic Technologies, Proteomics and Cell Biology at the All-Russia Research Institute for Agricultural Microbiology, of the Core Centrum Cellular and Molecular Technologies for the Study of Plants and Fungi in V.L. Komarov Botanical Institute, and the Molecular and Cell Technologies Research Resource Centre at Saint Petersburg State University.

Conflicts of Interest: The authors declare no conflict of interest.

References

1. Parniske, M. Intracellular accommodation of microbes by plants: A common developmental program for symbiosis and disease? *Curr. Opin. Plant Biol.* **2000**, *3*, 320–328. [[CrossRef](#)]
2. Courty, P.E.; Smith, P.; Koegel, S.; Redecker, D.; Wipf, D. Inorganic nitrogen uptake and transport in beneficial plant root-microbe interactions. *Crit. Rev. Plant Sci.* **2015**, *34*, 4–16. [[CrossRef](#)]
3. Peix, A.; Ramírez-Bahena, M.H.; Velázquez, E.; Bedmar, E.J. Bacterial associations with legumes. *Crit. Rev. Plant Sci.* **2015**, *34*, 17–42. [[CrossRef](#)]
4. Vaz Patto, M.C.; Amarowicz, R.; Aryee, A.N.; Boye, J.I.; Chung, H.-J.; Martín-Cabrejas, M.A.; Domoney, C. Achievements and challenges in improving the nutritional quality of food legumes. *Crit. Rev. Plant Sci.* **2015**, *34*, 105–143. [[CrossRef](#)]
5. Nakanishi, T.; Inada, A.; Kambayashi, K.; Yoneda, K. Flavonoid glycosides of the roots of *Glycyrrhiza uralensis*. *Phytochemistry* **1985**, *24*, 339–341. [[CrossRef](#)]
6. Zhang, C.-H.; Yu, Y.; Liang, Y.-Z.; Chen, X.-Q. Purification, partial characterization and antioxidant activity of polysaccharides from *Glycyrrhiza uralensis*. *Int. J. Biol. Macromol.* **2015**, *79*, 681–686. [[CrossRef](#)] [[PubMed](#)]
7. Zhang, Q.; Ye, M. Chemical analysis of the Chinese herbal medicine Gan-Cao (licorice). *J. Chromatogr. A* **2009**, *1216*, 1954–1969. [[CrossRef](#)]
8. Ramilowski, J.A.; Sawai, S.; Seki, H.; Mochida, K.; Yoshida, T.; Sakurai, T.; Muranaka, T.; Saito, K.; Daub, C.O. *Glycyrrhiza uralensis* transcriptome landscape and study of phytochemicals. *Plant Cell Physiol.* **2013**, *54*, 697–710. [[CrossRef](#)] [[PubMed](#)]
9. Liu, Y.; Zhang, P.; Song, M.; Hou, J.; Qing, M.; Wang, W.; Liu, C. Transcriptome analysis and development of SSR molecular markers in *Glycyrrhiza uralensis* Fisch. *PLoS ONE* **2015**, *10*, e0143017. [[CrossRef](#)]
10. Mochida, K.; Sakurai, T.; Seki, H.; Yoshida, T.; Takahagi, K.; Sawai, S.; Uchiyama, H.; Muranaka, T.; Saito, K. Draft genome assembly and annotation of *Glycyrrhiza uralensis*, a medicinal legume. *Plant J.* **2017**, *89*, 181–194. [[CrossRef](#)] [[PubMed](#)]

11. Kang, S.-H.; Lee, J.-H.; Lee, H.O.; Ahn, B.O.; Won, S.Y.; Sohn, S.-H.; Kim, J.S. Complete chloroplast genome and 45S nrDNA sequences of the medicinal plant species *Glycyrrhiza glabra* and *Glycyrrhiza uralensis*. *Genes Genet. Syst.* **2018**, *93*, 83–89. [[CrossRef](#)] [[PubMed](#)]
12. Yang, Y.-Y.; Li, S.-N.; Xu, L.; Xing, Y.-P.; Zhao, R.; Bao, G.-H.; Zhang, T.-T.; Zhang, D.-C.; Song, Y.-Y.; Ao, W.-L.; et al. The complete mitochondrial genome of *Glycyrrhiza uralensis* Fisch. (Fabales, Leguminosae). *Mitochondrial DNA B* **2021**, *6*, 475–477. [[CrossRef](#)] [[PubMed](#)]
13. Wu, S.; Yu, K.; Ding, X.; Song, F.; Liang, X.; Li, Z.; Peng, L. Transcriptomic analyses reveal dynamic changes of defense response in *Glycyrrhiza uralensis* leaves under enhanced ultraviolet-B radiation. *Plant Physiol. Biochem.* **2021**, *163*, 358–366. [[CrossRef](#)]
14. Wang, C.; Chen, L.; Cai, Z.; Chen, C.; Liu, Z.; Liu, S.; Zou, L.; Tan, M.; Chen, J.; Liu, X.; et al. Metabolite profiling and transcriptome analysis explains difference in accumulation of bioactive constituents in licorice (*Glycyrrhiza uralensis*) under salt stress. *Front. Plant Sci.* **2021**, *12*, 727882. [[CrossRef](#)] [[PubMed](#)]
15. Margaret-Oliver, I.; Lei, W.; Parada, M.; Rodríguez-Carvajal, M.A.; Crespo-Rivas, J.C.; Hidalgo, Á.; Gil-Serrano, A.; Moreno, J.; Rodríguez-Navarro, D.N.; Buendía-Clavería, A.; et al. *Sinorhizobium fredii* HH103 does not strictly require KPS and/or EPS to nodulate *Glycyrrhiza uralensis*, an indeterminate nodule-forming legume. *Arch. Microbiol.* **2012**, *194*, 87–102. [[CrossRef](#)] [[PubMed](#)]
16. Li, L.; Sinkko, H.; Montonen, L.; Wei, G.; Lindström, K.; Räsänen, L.A. Biogeography of symbiotic and other endophytic bacteria isolated from medicinal *Glycyrrhiza* species in China. *FEMS Microbiol. Ecol.* **2012**, *79*, 46–68. [[CrossRef](#)]
17. Margaret, I.; Crespo-Rivas, J.C.; Acosta-Jurado, S.; Buendía-Clavería, A.M.; Cubo, M.T.; Gil-Serrano, A.; Moreno, J.; Murdoch, P.S.; Rodríguez-Carvajal, M.A.; Rodríguez-Navarro, D.N.; et al. *Sinorhizobium fredii* HH103 *rkp-3* genes are required for K-antigen polysaccharide biosynthesis, affect lipopolysaccharide structure and are essential for infection of legumes forming determinate nodules. *Mol. Plant Microbe Interact.* **2012**, *25*, 825–838. [[CrossRef](#)]
18. Safronova, V.; Belimov, A.; Sazanova, A.; Chirak, E.; Kuznetsova, I.; Andronov, E.; Pinaev, A.; Tsyganova, A.; Seliverstova, E.; Kitaeva, A.; et al. Two broad host range rhizobial strains isolated from relict legumes have various complementary effects on symbiotic parameters of co-inoculated plants. *Front. Microbiol.* **2019**, *10*, 514. [[CrossRef](#)] [[PubMed](#)]
19. Guinel, F.C. Getting around the legume nodule: I. The structure of the peripheral zone in four nodule types. *Botany* **2009**, *87*, 1117–1138. [[CrossRef](#)]
20. Serova, T.A.; Tsyganova, A.V.; Tsyganov, V.E. Early nodule senescence is activated in symbiotic mutants of pea (*Pisum sativum* L.) forming ineffective nodules blocked at different nodule developmental stages. *Protoplasma* **2018**, *255*, 1443–1459. [[CrossRef](#)] [[PubMed](#)]
21. Chua, K.Y.; Pankhurst, C.E.; Macdonald, P.E.; Hopcroft, D.H.; Jarvis, B.D.; Scott, D.B. Isolation and characterization of transposon Tn5-induced symbiotic mutants of *Rhizobium loti*. *J. Bacteriol.* **1985**, *162*, 335–343. [[CrossRef](#)]
22. Hirsch, A.M.; Smith, C.A. Effects of *Rhizobium meliloti* *nif* and *fix* mutants on alfalfa root nodule development. *J. Bacteriol.* **1987**, *169*, 1137–1146. [[CrossRef](#)] [[PubMed](#)]
23. Chungopast, S.; Hirakawa, H.; Sato, S.; Handa, Y.; Saito, K.; Kawaguchi, M.; Tajima, S.; Nomura, M. Transcriptomic profiles of nodule senescence in *Lotus japonicus* and *Mesorhizobium loti* symbiosis. *Plant Biotechnol.* **2014**, *31*, 345–349. [[CrossRef](#)]
24. González, E.M.; Aparicio-Tejo, P.M.; Gordon, A.J.; Minchin, F.R.; Royuela, M.; Arrese-Igor, C. Water-deficit effects on carbon and nitrogen metabolism of pea nodules. *J. Exp. Bot.* **1998**, *49*, 1705–1714. [[CrossRef](#)]
25. Matamoros, M.A.; Baird, L.M.; Escuredo, P.R.; Dalton, D.A.; Minchin, F.R.; Iturbe-Ormaetxe, I.A.; Rubio, M.C.; Moran, J.F.; Gordon, A.J.; Becana, M. Stress-induced legume root nodule senescence. physiological, biochemical, and structural alterations. *Plant Physiol.* **1999**, *121*, 97–112. [[CrossRef](#)]
26. Pérez Guerra, J.C.; Coussens, G.; De Keyser, A.; De Rycke, R.; De Bodt, S.; Van De Velde, W.; Goormachtig, S.; Holsters, M. Comparison of developmental and stress-induced nodule senescence in *Medicago truncatula*. *Plant Physiol.* **2010**, *152*, 1574–1584. [[CrossRef](#)]
27. Tsyganova, A.V.; Kitaeva, A.B.; Tsyganov, V.E. Cell differentiation in nitrogen-fixing nodules hosting symbiosomes. *Funct. Plant Biol.* **2018**, *45*, 47–57. [[CrossRef](#)] [[PubMed](#)]
28. Prell, J.; Poole, P. Metabolic changes of rhizobia in legume nodules. *Trends Microbiol.* **2006**, *14*, 161–168. [[CrossRef](#)]
29. Vasse, J.; de Billy, F.; Camut, S.; Truchet, G. Correlation between ultrastructural differentiation of bacteroids and nitrogen fixation in alfalfa nodules. *J. Bacteriol.* **1990**, *172*, 4295–4306. [[CrossRef](#)]
30. Kitaeva, A.B.; Gorshkov, A.P.; Kirichek, E.A.; Kusakin, P.G.; Tsyganova, A.V.; Tsyganov, V.E. General patterns and species-specific differences in the organization of the tubulin cytoskeleton in indeterminate nodules of three legumes. *Cells* **2021**, *10*, 1012. [[CrossRef](#)]
31. Tsyganov, V.E.; Morzhina, E.V.; Stefanov, S.Y.; Borisov, A.Y.; Lebsky, V.K.; Tikhonovich, I.A. The pea (*Pisum sativum* L.) genes *sym33* and *sym40* control infection thread formation and root nodule function. *Mol. Gen. Genet.* **1998**, *259*, 491–503. [[CrossRef](#)] [[PubMed](#)]
32. Montiel, J.; Downie, J.A.; Farkas, A.; Bihari, P.; Herczeg, R.; Bálint, B.; Mergaert, P.; Kereszt, A.; Kondorosi, É. Morphotype of bacteroids in different legumes correlates with the number and type of symbiotic NCR peptides. *Proc. Natl. Acad. Sci. USA* **2017**, *114*, 5041–5046. [[CrossRef](#)] [[PubMed](#)]
33. Montiel, J.; Szűcs, A.; Boboescu, I.Z.; Gherman, V.D.; Kondorosi, É.; Kereszt, A. Terminal bacteroid differentiation is associated with variable morphological changes in legume species belonging to the inverted repeat-lacking clade. *Mol. Plant Microbe Interact.* **2016**, *29*, 210–219. [[CrossRef](#)] [[PubMed](#)]

34. Kitaeva, A.B.; Demchenko, K.N.; Tikhonovich, I.A.; Timmers, A.C.J.; Tsyganov, V.E. Comparative analysis of the tubulin cytoskeleton organization in nodules of *Medicago truncatula* and *Pisum sativum*: Bacterial release and bacteroid positioning correlate with characteristic microtubule rearrangements. *New Phytol.* **2016**, *210*, 168–183. [[CrossRef](#)] [[PubMed](#)]
35. Kusaba, I.; Nakao, T.; Maita, H.; Sato, S.; Chijiwa, R.; Yamada, E.; Arima, S.; Kojoma, M.; Ishimaru, K.; Akashi, R.; et al. *Mesorhizobium* sp. J8 can establish symbiosis with *Glycyrrhiza uralensis*, increasing glycyrrhizin production. *Plant Biotechnol.* **2021**, *38*, 57–66. [[CrossRef](#)]
36. Xie, W.; Hao, Z.; Zhou, X.; Jiang, X.; Xu, L.; Wu, S.; Zhao, A.; Zhang, X.; Chen, B. Arbuscular mycorrhiza facilitates the accumulation of glycyrrhizin and liquiritin in *Glycyrrhiza uralensis* under drought stress. *Mycorrhiza* **2018**, *28*, 285–300. [[CrossRef](#)] [[PubMed](#)]
37. Xie, W.; Hao, Z.; Yu, M.; Wu, Z.; Zhao, A.; Li, J.; Zhang, X.; Chen, B. Improved phosphorus nutrition by arbuscular mycorrhizal symbiosis as a key factor facilitating glycyrrhizin and liquiritin accumulation in *Glycyrrhiza uralensis*. *Plant Soil* **2019**, *439*, 243–257. [[CrossRef](#)]
38. Fähræus, G. The infection of clover root hairs by nodule bacteria studied by a simple glass slide technique. *J. Gen. Microbiol.* **1957**, *16*, 374–381. [[CrossRef](#)]
39. Humphrey, C.D.; Pittman, F.E. A simple methylene blue-azure II-basic fuchsin stain for epoxy-embedded tissue sections. *Stain Technol.* **1974**, *49*, 9–14. [[CrossRef](#)]
40. Kitaeva, A.B.; Kusakin, P.G.; Demchenko, K.N.; Tsyganov, V.E. Key methodological features of tubulin cytoskeleton studies in nodules of legume plants. *Sel'skokhozyaistvennaya Biol.* **2018**, *53*, 634–644. [[CrossRef](#)]
41. VandenBosch, K.A.; Bradley, D.J.; Knox, J.P.; Perotto, S.; Butcher, G.W.; Brewin, N.J. Common components of the infection thread matrix and the intercellular space identified by immunocytochemical analysis of pea nodules and uninfected roots. *EMBO J.* **1989**, *8*, 335–341. [[CrossRef](#)] [[PubMed](#)]
42. Phansalkar, N.; More, S.; Sabale, A.; Joshi, M. Adaptive Local Thresholding for Detection of Nuclei in Diversity Stained Cytology Images. In Proceedings of the 2011 IEEE International Conference on Acoustics, Speech and Signal Processing (ICASSP), Kerala, India, 10–12 February 2011; Institute of Electrical and Electronics Engineers: Piscataway, NJ, USA, 2011; pp. 218–220.
43. Schindelin, J.; Arganda-Carreras, I.; Frise, E.; Kaynig, V.; Longair, M.; Pietzsch, T.; Preibisch, S.; Rueden, C.; Saalfeld, S.; Schmid, B.; et al. Fiji: An open-source platform for biological-image analysis. *Nat. Methods* **2012**, *9*, 676–682. [[CrossRef](#)]
44. Jacques, E.; Buytaert, J.; Wells, D.M.; Lewandowski, M.; Bennett, M.J.; Dirckx, J.; Verbelen, J.P.; Vissenberg, K. MicroFilament Analyzer, an image analysis tool for quantifying fibrillar orientation, reveals changes in microtubule organization during gravitropism. *Plant J.* **2013**, *74*, 1045–1058. [[CrossRef](#)] [[PubMed](#)]
45. Brewin, N.J. Plant cell wall remodelling in the *Rhizobium*–legume symbiosis. *Crit. Rev. Plant Sci.* **2004**, *23*, 293–316. [[CrossRef](#)]
46. Crespo-Rivas, J.C.; Guefrachi, I.; Mok, K.C.; Villaécija-Aguilar, J.A.; Acosta-Jurado, S.; Pierre, O.; Ruiz-Sainz, J.E.; Taga, M.E.; Mergaert, P.; Vinardell, J.M. *Sinorhizobium fredii* HH103 bacteroids are not terminally differentiated and show altered O-antigen in nodules of the Inverted Repeat-Lacking Clade legume *Glycyrrhiza uralensis*. *Environ. Microbiol.* **2016**, *18*, 2392–2404. [[CrossRef](#)] [[PubMed](#)]
47. Rae, A.L.; Bonfante-Fasolo, P.; Brewin, N.J. Structure and growth of infection threads in the legume symbiosis with *Rhizobium leguminosarum*. *Plant J.* **1992**, *2*, 385–395. [[CrossRef](#)]
48. Tsyganova, A.V.; Seliverstova, E.V.; Brewin, N.J.; Tsyganov, V.E. Comparative analysis of remodelling of the plant–microbe interface in *Pisum sativum* and *Medicago truncatula* symbiotic nodules. *Protoplasma* **2019**, *256*, 983–996. [[CrossRef](#)] [[PubMed](#)]
49. Kereszt, A.; Mergaert, P.; Kondorosi, E. Bacteroid development in legume nodules: Evolution of mutual benefit or of sacrificial victims? *Mol. Plant Microbe Interact.* **2011**, *24*, 1300–1309. [[CrossRef](#)]
50. Ishihara, H.; Koriyama, H.; Osawa, A.; Zehirov, G.; Yamaura, M.; Kucho, K.-I.; Abe, M.; Higashi, S.; Kondorosi, E.; Mergaert, P.; et al. Characteristics of bacteroids in indeterminate nodules of the leguminous tree *Leucaena glauca*. *Microbes Environ.* **2011**, *26*, 156–159. [[CrossRef](#)] [[PubMed](#)]
51. Tsyganov, V.E.; Tsyganova, A.V.; Gorshkov, A.P.; Seliverstova, E.V.; Kim, V.E.; Chizhevskaya, E.P.; Belimov, A.A.; Serova, T.A.; Ivanova, K.A.; Kulaeva, O.A.; et al. Efficacy of a plant-microbe system: *Pisum sativum* (L.) cadmium-tolerant mutant and *Rhizobium leguminosarum* strains, expressing pea metallothionein genes *PsMT1* and *PsMT2*, for cadmium phytoremediation. *Front. Microbiol.* **2020**, *11*, 15. [[CrossRef](#)]
52. Tsyganova, A.V.; Seliverstova, E.V.; Tsyganov, V.E. Influence of mutation in pea (*Pisum sativum* L.) *cdt* (cadmium tolerance) gene on histological and ultrastructural nodule organization. *Ekol. Genet.* **2019**, *17*, 71–80. [[CrossRef](#)]
53. Gorshkov, A.P.; Tsyganova, A.V.; Vorobiev, M.G.; Tsyganov, V.E. The fungicide tetramethylthiuram disulfide negatively affects plant cell walls, infection thread walls, and symbiosomes in pea (*Pisum sativum* L.) symbiotic nodules. *Plants* **2020**, *9*, 1488. [[CrossRef](#)] [[PubMed](#)]
54. Vinardell, J.M.; Fedorova, E.; Cebolla, A.; Kevei, Z.; Horvath, G.; Kelemen, Z.; Tarayre, S.; Roudier, F.; Mergaert, P.; Kondorosi, E.; et al. Endoreduplication mediated by the anaphase-promoting complex activator CCS52A is required for symbiotic cell differentiation in *Medicago truncatula* nodules. *Plant Cell* **2003**, *15*, 2093–2105. [[CrossRef](#)]
55. Sinharoy, S.; Torres-Jerez, I.; Bandyopadhyay, K.; Kereszt, A.; Pislariu, C.I.; Nakashima, J.; Benedito, V.A.; Kondorosi, E.; Udvardi, M.K. The C₂H₂ transcription factor regulator of symbiosome differentiation represses transcription of the secretory pathway gene *VAMP721a* and promotes symbiosome development in *Medicago truncatula*. *Plant Cell* **2013**, *25*, 3584–3601. [[CrossRef](#)]

56. Feng, Z.; Zhang, L.; Wu, Y.; Wang, L.; Xu, M.; Yang, M.; Li, Y.; Wei, G.; Chou, M. The *Rpf84* gene, encoding a ribosomal large subunit protein, RPL22, regulates symbiotic nodulation in *Robinia pseudoacacia*. *Planta* **2019**, *250*, 1897–1910. [[CrossRef](#)]
57. Borisov, A.Y.; Rozov, S.M.; Tsyganov, V.E.; Morzhina, E.V.; Lebsky, V.K.; Tikhonovich, I.A. Sequential functioning of *Sym-13* and *Sym-31*, two genes affecting symbiosome development in root nodules of pea (*Pisum sativum* L.). *Mol. Gen. Genet.* **1997**, *254*, 592–598. [[CrossRef](#)] [[PubMed](#)]
58. Sherrier, D.J.; Borisov, A.Y.; Tikhonovich, I.A.; Brewin, N.J. Immunocytological evidence for abnormal symbiosome development in nodules of the pea mutant line Sprint-2Fix⁻ (*sym31*). *Protoplasma* **1997**, *199*, 57–68. [[CrossRef](#)]
59. Novák, K.; Pešina, K.; Nebesářová, J.; Škrdleta, V.; Lisá, L.; Našinec, V. Symbiotic tissue degradation pattern in the ineffective nodules of three nodulation mutants of pea (*Pisum sativum* L.). *Ann. Bot.* **1995**, *76*, 303–313. [[CrossRef](#)]
60. Morzhina, E.V.; Tsyganov, V.E.; Borisov, A.Y.; Lebsky, V.K.; Tikhonovich, I.A. Four developmental stages identified by genetic dissection of pea (*Pisum sativum* L.) root nodule morphogenesis. *Plant Sci.* **2000**, *155*, 75–83. [[CrossRef](#)]
61. Oono, R.; Denison, R.F. Comparing symbiotic efficiency between swollen versus nonswollen rhizobial bacteroids. *Plant Physiol.* **2010**, *154*, 1541–1548. [[CrossRef](#)] [[PubMed](#)]
62. Ludwig, E.M.; Leonard, M.; Marroqui, S.; Wheeler, T.R.; Findlay, K.; Downie, J.A.; Poole, P.S. Role of polyhydroxybutyrate and glycogen as carbon storage compounds in pea and bean bacteroids. *Mol. Plant Microbe Interact.* **2005**, *18*, 67–74. [[CrossRef](#)]
63. Trainer, M.A.; Charles, T.C. The role of PHB metabolism in the symbiosis of rhizobia with legumes. *Appl. Microbiol. Biotechnol.* **2006**, *71*, 377–386. [[CrossRef](#)] [[PubMed](#)]
64. Pankhurst, C.E.; Craig, A.S.; Jones, W.T. Effectiveness of *Lotus* root nodules: I. Morphology and flavon content of nodules formed on *Lotus pedunculatus* by fast-growing *Lotus* rhizobia. *J. Exp. Bot.* **1979**, *30*, 1085–1093. [[CrossRef](#)]
65. Sujkowska-Rybkowska, M.; Kasowska, D.; Gediga, K.; Banasiewicz, J.; Stępkowski, T. *Lotus corniculatus*-rhizobia symbiosis under Ni, Co and Cr stress on ultramafic soil. *Plant Soil* **2020**, *451*, 459–484. [[CrossRef](#)]
66. Crowell, E.F.; Gonneau, M.; Vernhettes, S.; Höfte, H. Regulation of anisotropic cell expansion in higher plants. *C. R. Biol.* **2010**, *333*, 320–324. [[CrossRef](#)] [[PubMed](#)]
67. Hamada, T. Microtubule Organization and Microtubule-Associated Proteins in Plant Cells. In *International Review of Cell and Molecular Biology*; Jeon, K.W., Ed.; Academic Press: Boston, MA, USA, 2014; Volume 312, pp. 1–52.